

## Novel SnO<sub>2</sub> / Mesoporous Carbon Spheres Composite Anode for Li-ion Batteries

Francesca Di Lupo<sup>1</sup>, Claudio Gerbaldi<sup>1,2,\*</sup>, Giuseppina Meligrana<sup>1</sup>, Silvia Bodoardo<sup>1,3</sup>, Nerino Penazzi<sup>1,3</sup>

<sup>1</sup> Department of Materials Science and Chemical Engineering, Politecnico di Torino; C.so Duca degli Abruzzi 24, 10129 Torino, Italy

<sup>2</sup> Center for Space Human Robotics @Polito, Italian Institute of Technology; Corso Trento 21, 10129 Torino, Italy

<sup>3</sup> INSTM UdR Politecnico di Torino; C.so Duca degli Abruzzi 24, 10129 Torino, Italy

\*E-mail: [claudio.gerbaldi@iit.it](mailto:claudio.gerbaldi@iit.it); [claudio.gerbaldi@polito.it](mailto:claudio.gerbaldi@polito.it)

Received: 7 June 2011 / Accepted: 11 July 2011 / Published: 1 August 2011

---

This work describes the preparation of a novel composite material made of nanosized SnO<sub>2</sub> supported into ordered mesoporous carbon spheres (SnO<sub>2</sub>/MCS) through a two-step hydrothermal/impregnation method. The morphology, structure and composition of the samples have been characterized by means of atomic emission spectroscopy, powder X-ray diffraction, scanning electron microscopy and nitrogen-adsorption techniques. The experimental findings suggest that the supported tin oxide species, with loading amounts as high as 30 wt. %, are located and dispersed onto the mesopores of the carbon spheres. Cyclic voltammetry and galvanostatic discharge/charge cycling have been used to test the electrochemical behaviour as anodes in test cells using lithium foils as both the counter and the reference electrodes. The best electrode cycles with a specific capacity in the order of 500 mAh g<sup>-1</sup> at C/10 current rate. It also performs well at high rate (1C rate), showing good capacity and excellent charge-discharge efficiency.

---

**Keywords:** SnO<sub>2</sub>; mesoporous carbon; anode material; lithium ion battery

### 1. INTRODUCTION

Li-ion battery systems are the state-of-the-art power sources for modern high-end consumer electronic products such as smart phones, tablet PCs and notebooks, offering high energy density, flexible and light-weight design, and extended cycle life. Large-scale Li-ion batteries have undergone a rapid and substantial improvement of the performances and they are currently in the forefront of the contenders for electric vehicles (EVs) and load-leveiling applications [1]. In such scenario, the power

and energy requirements cannot be met with the current choices of electrode materials, especially for the anode [2]. Graphite is the standard active material found in commercial Li-ion cells at the anode side; nevertheless its theoretical specific capacity is limited to about 370 mAh g<sup>-1</sup> [3,4], while metal storage alloys and intermetallics have a potential capacity of 1000-2000 mAh g<sup>-1</sup> [5].

Tin-based materials, particularly tin oxides [6], have been widely investigated since 1997 as potential graphite substitutes mainly on the basis of their high theoretical specific capacity around 790 mAh g<sup>-1</sup>, low-cost, safety and low discharge plateau [7-9]. However, in spite of its considerable advantages, the practical implementation of SnO<sub>2</sub> is hampered by poor material cyclability arising from the large volume expansion-contraction experienced during repeated charge/discharge cycling processes, which causes electrode material pulverization and the loss of electrical contact [10]. Furthermore, SnO<sub>2</sub> has poor electronic conductivity; meaning that it must be intimately contacted with electronically conductive additives. A way to solve these problems is to downsize the Li storage material particles to a nanoscale level and to use a "buffer matrix" to avoid volume expansion during the lithium alloying and de-alloying processes [11]. Several studies have been focused on SnO<sub>2</sub>/carbon composites [12,13] because carbon can offer a higher interfacial area for transportation of both lithium ions and electrons; moreover, it serves as a barrier to Sn particle agglomeration and provides the space to buffer the volume changes. Among various carbon materials, ordered mesoporous carbon spheres (MCS) have been reported to show good performances because of their high thermal stability, large surface area, uniform pore diameter, high pore volume and interconnected pore structure [4,14]. Moreover, as graphitic carbon has a higher electronic conductivity, it is naturally interesting to determine whether the performance of SnO<sub>2</sub> in mesoporous carbon spheres can be further improved by increasing the degree of graphitization of the support.

In this work, a novel SnO<sub>2</sub>/MCS composite material is prepared by using phenanthrene as carbon precursor in order to increase the degree of graphitization of the carbon support. A two-step efficient and facile hydrothermal/impregnation method is used to the purpose. The electrochemical behaviour is compared with a SnO<sub>2</sub>/MCS composite, where mesoporous carbon spheres are prepared using the commonly used sucrose carbon precursor. It is herein demonstrated that the newly developed composite can release superior cycle performance and a good rate capability when it served as negative electrode in test cell using lithium as the counter electrode.

## 2. EXPERIMENTAL PART

### 2.1. Synthesis of SnO<sub>2</sub>/MCS composite

The SnO<sub>2</sub>/MCS composites were obtained by a simple low cost preparation, based on the hydrothermal synthesis of a silica template (SBA-15), the template conversion into the carbon replica (CMK-3) and, finally, the dispersion of the oxide particles by wetness impregnation followed by heat treatment.

Hexagonally ordered SBA-15 mesoporous silica spheres were firstly synthesized following the procedure described by Katiyar et al. [15], using tetraethyl orthosilicate (TEOS, Fluka), Pluronic P123

triblock co-polymers (EO<sub>20</sub>-PO<sub>70</sub>-EO<sub>20</sub>, Aldrich), hexadecyltrimethylammonium bromide (CTAB, Aldrich), hydrochloric acid (HCl 37 wt. %, Fluka), ethanol (C<sub>2</sub>H<sub>6</sub>O 100 %, Fluka) and doubly distilled water as reactants.

One gram of calcined SBA-15 was used to synthesize the CMK-3 carbon replica, by using phenanthrene as carbon source. MCS-P (carbon replica from phenanthrene precursor) was synthesized by impregnating the SBA-15 with phenanthrene (Aldrich) in slight acidic conditions (p-toluene sulfonic acid monohydrate in acetone, both obtained by Aldrich), followed by a two-step heating process at 100 and 160 °C, respectively, for 6 h to carbonise the phenanthrene. The impregnation-drying step was repeated twice to completely infiltrate the internal pores of SBA-15 template with carbon. Carbonisation was completed by pyrolysis at 950 °C under nitrogen flow. After pyrolysis, a carbon-silica composite was obtained.

A 10 wt. % HF (Aldrich) in water-ethanol solution was used for completely remove silica, thus obtaining a dark brown powder of mesoporous carbon spheres. For comparison, a MCS-S (carbon replica from sucrose precursor) was similarly prepared but using, in this case, sucrose (Aldrich), sulphuric acid and doubly distilled water [16].

Dispersion of the alloying metal onto the mesopores of the MCSs was achieved by the wetness impregnation technique [11,17]: a solution of SnCl<sub>2</sub> (anhydrous, Fluka) in ethanol was firstly prepared, in which MCSs were soaked. The resulting suspension was stirred for 30 min, and then sonicated for 30 min. Finally, the solvent was slowly evaporated heating at 55 °C overnight, with continuous stirring. The obtained powder was heated in flowing Ar at 350 °C and kept for 4 hours at the same temperature. The samples obtained are hereafter denoted as SnO<sub>2</sub>/MCS-P and SnO<sub>2</sub>/MCS-S.

## 2.2. Chemical and structural characterization

Quantitative elemental analysis was carried out by inductively coupled plasma-atomic emission spectroscopy (ICP-AES) with a Varian Liberty 100 instrument. Prior to analysis, samples were digested in hot concentrated HCl:HNO<sub>3</sub> = 3:1 mixture.

The X-ray diffraction profiles of the samples were obtained using a Philips Xpert MPD powder diffractometer, equipped with Cu K $\alpha$  radiation (V = 40 kV, i = 30 mA) and a curved graphite secondary monochromator.

The diffraction profiles were collected in the  $2\theta$  range between 0.5° and 4° for the low diffraction angles patterns and between 10° and 80° for the high diffraction angles patterns, both with an acquisition step of 0.02° and a time per step of 10 s. The samples were also submitted to scanning electron microscope (SEM) investigation for morphological characterization, using a FEI Quanta Inspect 200LV scanning electron microscope (SEM, max magnification of 1.5×10<sup>5</sup>) equipped with an energy-dispersive X-ray analyzer EDAX Genesis system with SUTW detector. Specific surface areas (SSA) were determined using the Brunauer, Emmet, Teller (BET) method on an ASAP 2010 Micromeritics instrument. Prior to adsorption, approximately 50.0 mg of solid were placed in the cell and evacuated at 300 °C for 3 hours under high vacuum. The pore diameter distribution was evaluated

by the Barrett-Joyner-Halenda (BJH) method, with the corrected form of the Kelvin equation, from desorption branches of the isotherms.

### 2.3. Electrochemical testing

The composition of the electrodes (area  $0.785\text{ cm}^2$ , weight about 2 mg) was: 82 wt. % of active material mixed with 10 wt. % of carbon black (Shawinigan Black AB50, Chevron Corp., USA) as electronic conductor and 8 wt. % poly(vinylidene fluoride) (PVdF, Solvay Solef 6020) as binder. The electrochemical response of the samples was tested in a polypropylene three-electrode T-cell assembled as follows: a working electrode formed by the given composition deposited on a copper foil (which acted as current collector), a 1.0 M lithium hexafluorophosphate ( $\text{LiPF}_6$ , Aldrich) in a 1:1 w/w % mixture of ethylene carbonate (EC, Fluka) and diethyl carbonate (DEC, Aldrich) electrolyte solution soaked on a Whatman<sup>®</sup> GF/A separator and a lithium metal foil (high purity lithium foils, Chemetall Foote corporation) as the counter electrode. When needed (i.e., for cyclic voltammetry), a lithium foil was added at the third opening, in direct contact to the electrolyte, acting as the reference electrode. The evaluation of the electrochemical performances was carried out by galvanostatic discharge/charge cycling (cut off voltages: 0.02 – 1.2 V vs.  $\text{Li}/\text{Li}^+$ ) and cyclic voltammetry (between 0.02 and 1.5 V vs.  $\text{Li}/\text{Li}^+$ , scan rate of  $0.100\text{ mV s}^{-1}$ ) at ambient temperature, using an Arbin Instrument Testing System model BT-2000 as the controlling instrument. The discharge/charge cycles were set at the same rate ranging from C/10 to 1C. In particular, discharge refers to the lithium alloying/insertion process, while charge refers to the de-alloying/de-insertion process.

## 3. RESULTS

### 3.1. Chemical, structural and morphological results

In order to unravel the composition and structure of the prepared samples, powder X-ray diffraction (XRD) experiments were carried out. The corresponding small-angle XRPD patterns are reported in Fig. 1a: mesoporous SBA-15 silica spheres (black line) used as template, its carbon replica MCS-P (red line) obtained using phenanthrene as carbon precursor and  $\text{SnO}_2/\text{MCS-P}$  (blue line) loaded with the tin oxide active material. The SBA-15 pattern shows three well-resolved peaks at  $2\theta = 0.87$ ,  $1.52$  and  $1.75$ , respectively, that are indexable as (100), (110) and (200) reflections associated with  $p6mm$  hexagonal symmetry. The two additional weak peaks in the  $2\theta$  range between  $2.0^\circ$  and  $3.0^\circ$  correspond to the (210) and (220) scattering reflections, indicating that the synthesized SBA-15 has a high degree of hexagonal mesoscopic organization [18]. The intense (100) peak reflects a  $d$  spacing of  $101.5\text{ \AA}$ . In consequence of the carbonization process and removal of the silica template, the XRD pattern for MCS-P (see Fig. 1, red line) shows that the  $p6mm$  morphology is preserved, although the diffraction peaks appear at slightly larger  $2\theta$  values, shifted to  $0.93^\circ$ , due to a slight framework shrinkage, reflecting a  $d$  spacing of  $95.0\text{ \AA}$ . The (110) and (200) peaks are less pronounced but still

clearly evident, indicating the long range ordering of the obtained mesoporous carbon material which retains a highly ordered hexagonal structure.

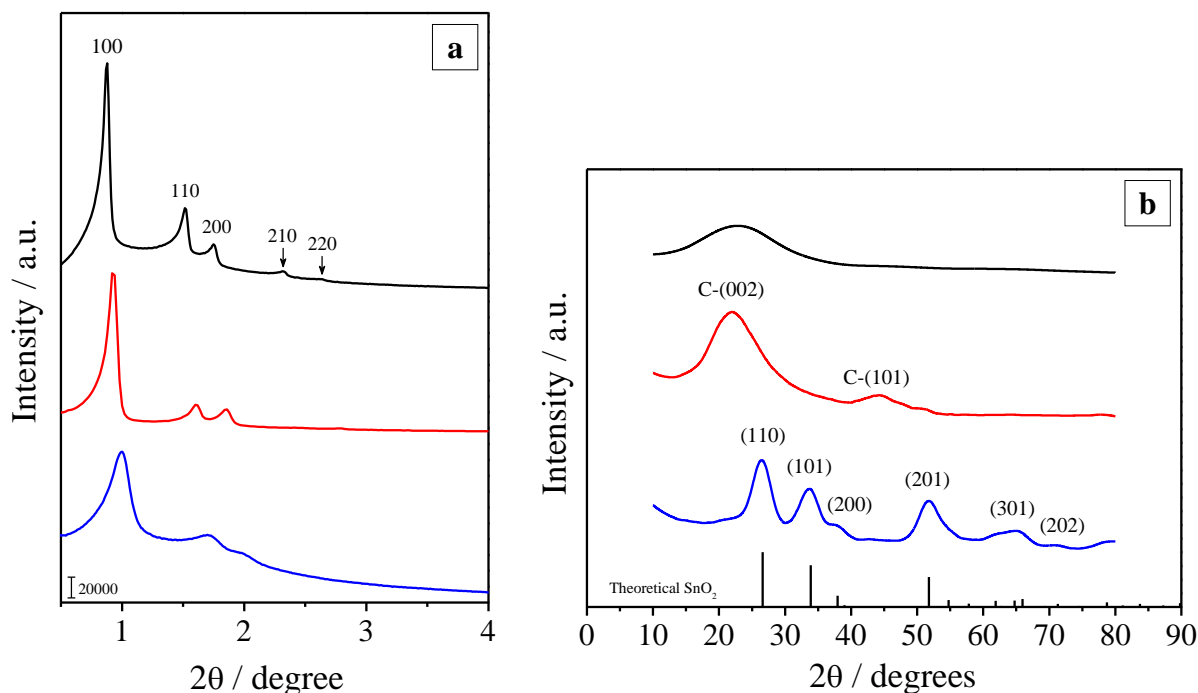


**Figure 1.** a) Small angle X-ray powder diffraction patterns of mesoporous SBA-15 spheres (black line), MCS-P (red line), and SnO<sub>2</sub>/MCS-P (blue line), respectively. b) Corresponding wide angle X-ray powder diffraction patterns.

The loading of SnO<sub>2</sub> onto the mesopores of MCS-P leads to a decrease in the intensity of the diffraction lines and a slight shift of the diffraction peaks to higher  $2\theta$  values (see Fig. 1, blue line). The decrease of XRD intensities is not attributed to a loss of long-range hexagonal structure upon impregnation with SnO<sub>2</sub>, but most likely to a change in the scattering density contrast. This is an indication of a partial filling of the mesopores by SnO<sub>2</sub>. All the characteristics of pristine SBA-15, in particular a high mesoporous order, are well maintained even after the SnO<sub>2</sub> loading. For all the three samples, the (100) Bragg reflections can be indexed with a hexagonal unit cell:  $a_0 = 117.2 \text{ \AA}$  ( $a_0 = 2d_{100}/\sqrt{3}$ ) for calcined SBA-15,  $a_0 = 109.7 \text{ \AA}$  for MCS-P, and  $a_0 = 102.0 \text{ \AA}$  for SnO<sub>2</sub>/MCS-P, respectively (see Table 1). The near retention of the unit cell indicates that the structure is maintained even upon the loading of SnO<sub>2</sub>, confirming the high stability of the MCS support.

The X-ray powder diffraction patterns at higher angles ( $2\theta = 10 - 80^\circ$ ) are shown in Fig. 1b. In the case of SBA-15 (black line), only the broad reflection of the amorphous silica wall-structure can be detected. According to index JCPDS Card No. 75-1621, the precursor material phenanthrene is decomposed under the given reaction condition to form MCS-P carbon. This is demonstrated by the presence of two broad peaks above  $20^\circ$  (see red line in Fig. 1b). Indeed, the (002) and (101) diffraction planes of hexagonal graphite are clearly visible. However, the broadening of the peaks indicates that the degree of graphitization in the product is not much pronounced. In the pattern of SnO<sub>2</sub>/MCS-P

(blue line) highly broadened peaks are clearly visible, well assigned to the tetragonal crystalline phase of rutile SnO<sub>2</sub> (JCPDS No. 41-1445), belonging to the space group  $P4_2/mnm$ . The scattering domains are very small, the crystallite size being between 30 and 40 Å, estimated using the Debye Scherrer formula. This value is slightly lower than the one obtained for the average pore size in MCS-P by BJH: these results allow considering that the SnO<sub>2</sub> particles could be most likely located inside the mesopores, dispersed on the wall surface of the channels. However, from the analysis of the XRD data SnO<sub>2</sub> particles should be also present outside the mesoporous structure of the support, in the form of crystallites with very small size.

**Table 1.** Comparative table of results from XRD, N<sub>2</sub> sorption experiments and ICP-AES analysis.

Sample	d <sub>100</sub> (Å)	a <sub>0</sub> (Å)	Specific surface area (m <sup>2</sup> g <sup>-1</sup> )	Desorption pore diameter (Å)	SnO <sub>2</sub> content (wt. %)
SBA-15	101.5	117.2	890	61.3	–
MCS-P	95.0	109.7	1070	50.2	–
SnO <sub>2</sub> /MCS-P	88.3	102.0	459	35.2	30.2

Nitrogen adsorption/desorption isotherms were used to study the changes induced in the textural properties in the different steps of the active material preparation, evaluating changes of the specific surface area and pore volume. Representative N<sub>2</sub> adsorption/desorption isotherms at 77 K are shown in Fig. 2 for the mesoporous SBA-15 silica material (black curve), its carbon replica MCS-P (red curve) and SnO<sub>2</sub>/MCS-P (blue curve).

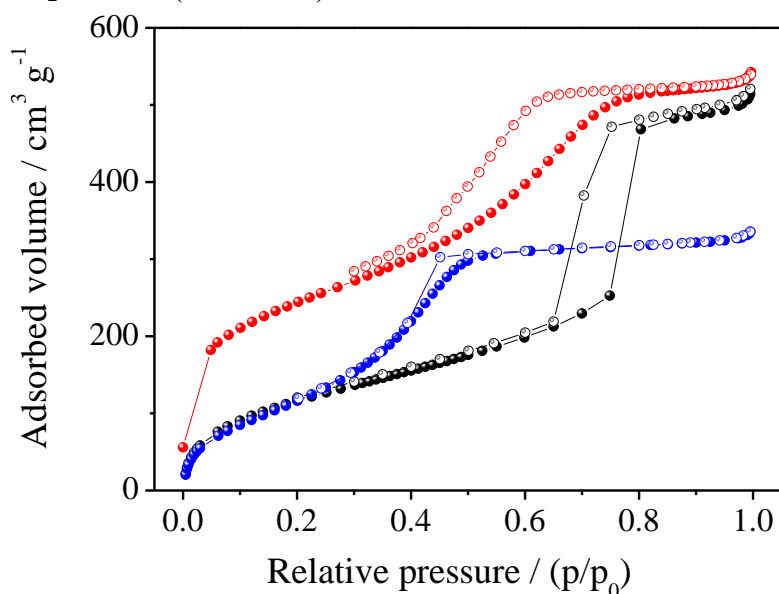


**Figure 2.** Adsorption/desorption isotherms of N<sub>2</sub> at 77K on mesoporous SBA-15 spheres (black curve), MCS-P (red curve), and SnO<sub>2</sub>/MCS-P (blue curve).

Table 1 summarizes the porous properties of synthesized materials determined from X-ray powder diffraction, BET (Brunauer, Emmett, and Teller) specific surface area and BJH (Barret-Joyner-Halenda) average pore diameter data obtained. All the results match very well with those reported in the literature and present a type-IV isotherm (IUPAC classification [19]), as it is expected for mesoporous systems. For SBA-15 (black curve) three well-distinguished regions of the adsorption isotherm are evident: a monolayer-multilayer adsorption, a capillary condensation, and a multilayer adsorption on the outer particles surface. A clear H1-type hysteresis loop is observed, which is typical of mesoporous materials with one-dimensional cylindrical channels [18,20], and the capillary condensation occurs at a  $p/p_0$  between 0,65 and 0,75. The sharpness of the inflection in this isotherm corresponds to capillary condensation within quite uniform and well definite mesopores, reflecting the uniform pore size in this material.

In the case of the MCS-P carbon replica (red curve), the amount of physisorbed gas is slightly increased, due to a larger specific surface. Furthermore, mesoporous carbon spheres have narrow pore size distributions with respect to the silica material since they are obtained as an inverse replica of the SBA-15 template: for this reasons the inflection due to capillary condensation is shifted towards lower pressure values, in the range  $p/p_0 = 0,4 - 0,7$ . The uniformity of the pore size is also lower, as demonstrated by the lower sharpness of the inflection. The specific surface area value obtained for MCS-P (i.e.,  $1070 \text{ m}^2 \text{ g}^{-1}$ , see Table 1) is similar to what reported in literature [21] for mesoporous carbons obtained starting from carbon precursors different from sucrose and could be due to the different graphitic character. Indeed, starting from an aromatic precursor such as phenanthrene it is expected to obtain a more graphitic carbon. The characteristics of the isotherm for the MCS-P supported with  $\text{SnO}_2$  (blue curve in Fig. 2) is similar to the one obtained for the unsupported material. However, the amount of physisorbed gas is strongly reduced, due to a smaller specific surface area (i.e.,  $459 \text{ m}^2 \text{ g}^{-1}$ , see Table 1). The sharp inflection due to capillary condensation is also slightly shifted towards lower pressure values, indicating a smaller pore size. As a result,  $\text{SnO}_2$  particles should be mainly encapsulated in the pore channels of the ordered mesoporous carbon. Reversible adsorption/desorption of nitrogen is still clearly visible, thus indicating that there is negligible obstruction of the pores [22,23].

The tin to carbon weight percentage in sample  $\text{SnO}_2/\text{MCS-P}$  was determined by means of ICP-AES elemental analysis. The results are reported in Table 1, showing that the obtained value (i.e., 30,02) is not too far from the value of 32 wt. %, expected on the basis of the amount of tin precursor used. No silicon was detected during the analysis, meaning that the silica core was completely removed.

The materials were then subjected to scanning electron microscopy (SEM) analysis for the morphological characterisation. The SEM micrographs, reported in Fig. 3, put in evidence the morphology of the MCS-P and  $\text{SnO}_2/\text{MCS-P}$  samples. The MCS-P support (Fig. 3A-C) presents regular spherical morphology; the particles are very homogeneous in shape and quite homogeneous in size (average particle size ranging from about 7 to 10  $\mu\text{m}$ ). After the wetness impregnation process (Fig. 3D-F), the observed morphology and the particle size do not significantly change. Furthermore, the surface of the spheres is found to be rougher but “clean”: no obvious big irregular agglomerates were observed on the external surface, indicating a good dispersion of tin oxide in the form of

nanoparticles, almost completely inside the mesoporous structure of MCS-P. Work is in progress in order to support this suggestion by means of TEM analysis.

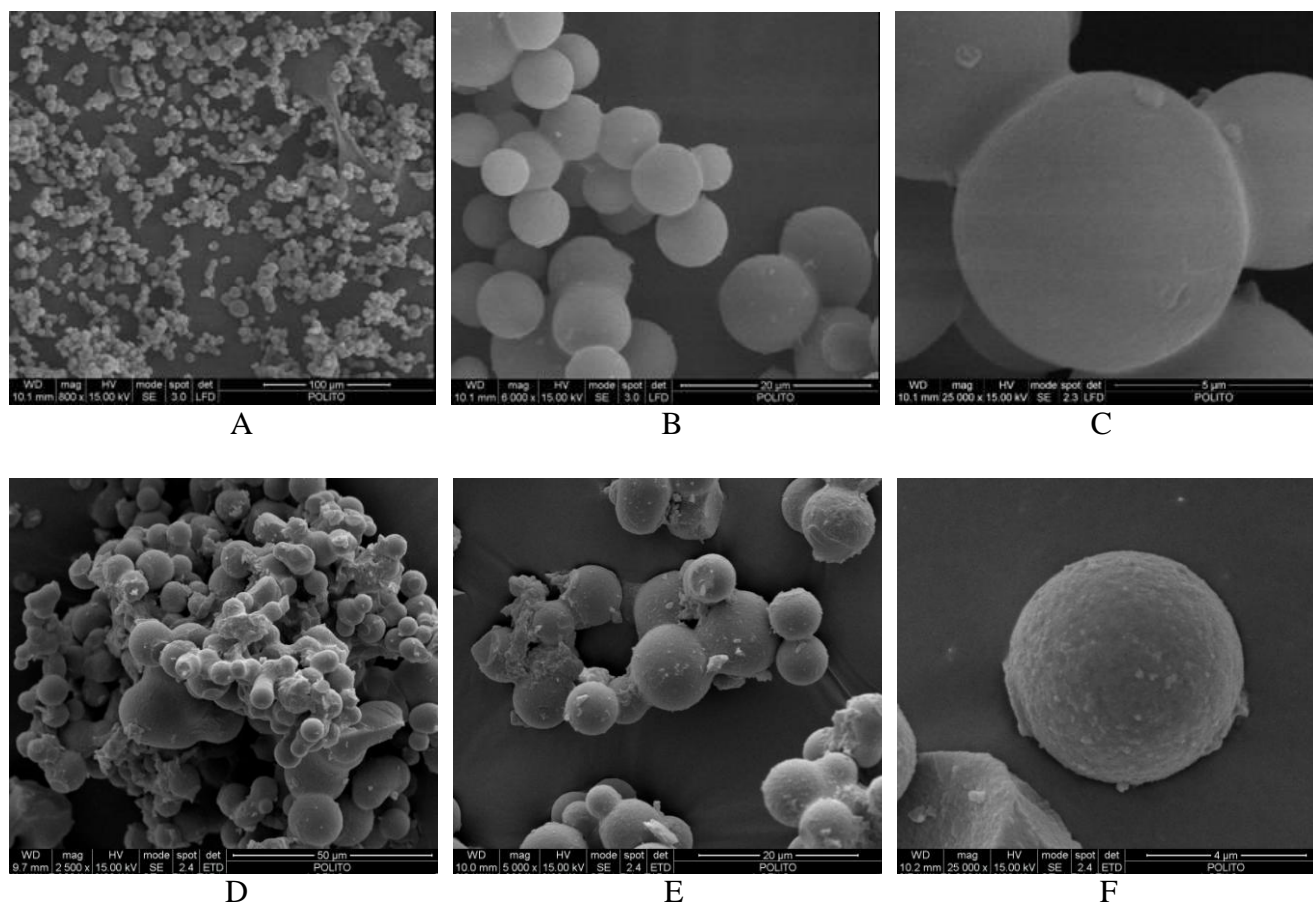


**Figure 3.** SEM micrographs of sample MCS-P (A–C) and sample SnO<sub>2</sub>/MCS-P (D–F).

To further confirm the composition of the sample, we carried out energy-dispersive X-ray (EDX) spectrum and elemental mapping characterization on different areas. The analysis confirmed the good dispersion of the active metal oxide: the peaks of C, O and Sn have been obviously identified. The EDX spectrum analysis of the spheres also tentatively provided a quantity of tin oxide of about 30-35 wt. % in the SnO<sub>2</sub>/MCS-P sample, which is consistent with the result of ICP-AES analysis.

### 3.2. Electrochemical results

The electrochemical behaviour of the synthesized SnO<sub>2</sub> supported MCS-P sample as anode for Li-ion batteries was tested via cyclic voltammetry (CV) and galvanostatic discharge/charge cycles. Tin oxides have a two-step reaction with lithium, as already stated in the literature [6]. Generally, the initial step involves the irreversible reduction of Sn oxide to Sn metal particles in a Li<sub>2</sub>O matrix, while the second step is the reversible alloying of Li<sup>+</sup> ions into the tin metal to form Li<sub>x</sub>Sn with  $x = 4.4$  max [24]. Fig. 4 shows the CV of the SnO<sub>2</sub>/MCS-P electrode (blue line) in the three-electrode cell having a

Li counter and a Li reference. The potential scanning began towards the decreasing potential branch, choosing as starting value the open circuit voltage (OCV = 2.9 V vs. Li/Li<sup>+</sup>) of the cell.

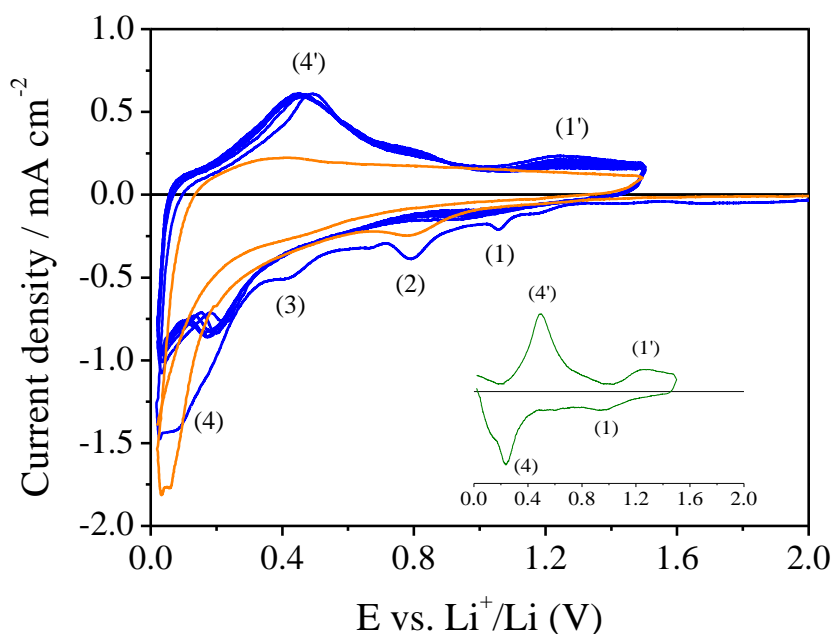


**Figure 4.** Cyclic voltammetry of the SnO<sub>2</sub>/MCS-P sample (blue line) compared with the MCS-P support (orange line). Scan rate = 0.100 mV s<sup>-1</sup> and voltage range = 0.02 – 1.5 V vs. Li/Li<sup>+</sup>.

One may notice the substantial difference between the first and the following cycles, revealing that the main electrochemical process is preceded by a series of secondary processes. Indeed, the first cathodic scan reveals a peak at above 1.0 V vs. Li/Li<sup>+</sup> (1), associated to the reduction of SnO<sub>2</sub> into metallic Sn and Li<sub>2</sub>O, as already stated by Liu et al. [25]. This peak is still visible in the subsequent cycles with decreased intensity and slightly shifted towards lower potential values. Moreover, a broad anodic peak centred at about 1.3 V vs. Li/Li<sup>+</sup> (1') can be also observed after the first cycle, which is most likely due to the partially reversible nature of this process, meaning that the lithium reaction with SnO<sub>2</sub> can be reversible to a certain extent [26-28]. The irreversible peak centred at about 0.8 V vs. Li/Li<sup>+</sup> (2) is reasonably associated with the decomposition of the electrolyte solvent with the formation of a passivating film on the electrode surface. This interpretation is supported by the peak potential position, whose value is typical of that generally associated with electrolyte decomposition and formation of a solid electrolyte interface (SEI) film [29]. Another confirmation comes by the comparison with the CV curve of the MCS-P support (orange line in Fig. 4) in which the same irreversible peak can be found at the same potential position. The broad current peaks observed between 0.5 and 0.02 V vs. Li/Li<sup>+</sup> can be ascribed to the formation of different alloy phases leading to the final Li<sub>x</sub>Sn alloy [25]. Peak (3), occurring at about 0.4 V vs. Li/Li<sup>+</sup>, can be tentatively associated with the reduction of some synthesis residuals that were still present in the SnO<sub>2</sub>/MCS matrix. All the above discussed peaks have no correspondence in the following anodic scan and, thus, they contribute to the high initial irreversible capacity observed in the galvanostatic alloying/de-alloying curves of the

SnO<sub>2</sub>/MCS-P electrode (see Fig. 5a,b). At the following voltammetric cycles, the cathodic branch shows marked modifications: peak (4) found at about 0.1 V vs. Li/Li<sup>+</sup> in the first cycle falls at 0.2 V vs. Li/Li<sup>+</sup> and its intensity is reduced, peak (3) and (2) are no more detectable, while peak (1) is substituted by a low intensity broad peak. Peak (4) is reflected by a broad peak in the following anodic scan (4'). All the subsequent cycles are reproducible and, thus, representative of the reversible electrode process. From the second cycle, the voltammetric characteristics remain unchanged.

To confirm these findings, the voltammetric characteristic of the pristine MCS-P carbon support has been recorded (see orange line in Fig. 4). It shows that no major contribution to the total electrode process comes from the support. Moreover, by subtracting the second voltammetric cycle of the MCS-P carbon from the corresponding one of the SnO<sub>2</sub> supported electrode, its contribution to the total electrochemical process is eliminated. The corresponding curve is shown in the inset of the same Fig. 4 (olive line). As clearly evident, while processes (1,1') and (4,4') appear more clearly, processes (2) and (3) practically disappear, becoming too faint to be related to any reversible process regarding the active material whatsoever. In fact, these are irreversible reactions taking place at the initial stages of the whole process, then disappearing during the following cycles.

The electrochemical behaviour in terms of discharge/charge galvanostatic cycling of this novel SnO<sub>2</sub>/MCS-P material has been tested in a cell using lithium metal as the counter electrode and a 1.0 M LiPF<sub>6</sub> in EC-DEC solution as the electrolyte. Some representative discharge and charge profiles at different current regimes are reported in Fig. 5a. The voltage profiles are characteristic of SnO<sub>2</sub>-based materials. The curves have the characteristic S-type shape centred at an average potential of 0.4 V vs. Li/Li<sup>+</sup>. The difference between the initial and the subsequent discharge profiles is likely due to the series of irreversible processes already discussed in the CV, mainly the decomposition of the electrolyte with the formation of an irreversible SEI layer. Another reason for the poor initial Coulombic efficiency is the large irreversible Li-ion insertion capacity contributed by the mesoporous carbon support [24].

Fig. 5b shows the discharge/charge specific capacity versus cycle number for the SnO<sub>2</sub>/MCS-P electrode, along with its Coulombic efficiency. In general, the sample shows good cyclability even at a high current regime. The initial reversible specific capacity at C/10 is found to be higher than 460 mAh g<sup>-1</sup>. After the initial cycles, the Coulombic efficiency rapidly increases to about 95 % and, subsequently, to above 98 %, then remaining stable throughout the cycles, indicating that the formed surface film remained intact and showed excellent reversible cycling after the surface reactions were completed. The reversible capacity after 10 cycles at C/10 is about 445 mAh g<sup>-1</sup>, which corresponds to 96 % retention of the initial capacity. Moreover, it can be found that our SnO<sub>2</sub>/MCS-P anode exhibits an interesting specific capacity of about 270 mAh g<sup>-1</sup> after 50 cycles at high 1C current rate, with retention of about 60 %. Also, the Coulombic efficiency remains steady at more than 99 % indicating excellent reversibility.

The maximum theoretical specific capacity that can be reached by this kind of electrode has been calculated to be 496 mAh g<sup>-1</sup>, considering the real amount of SnO<sub>2</sub> obtained by ICP-AES (i.e., 30.2 wt. %) and assuming that the mesoporous carbons (69.8 wt. %) have the capacity of graphite: 260 mAh g<sup>-1</sup> from the MCS-P support (69.8 % of 372 mAh g<sup>-1</sup>, i.e. the theoretical specific

capacity of graphite) and 236 mAh g<sup>-1</sup> from SnO<sub>2</sub> (30.2 % of 780 mAh g<sup>-1</sup>, i.e. the theoretical specific capacity of SnO<sub>2</sub>).

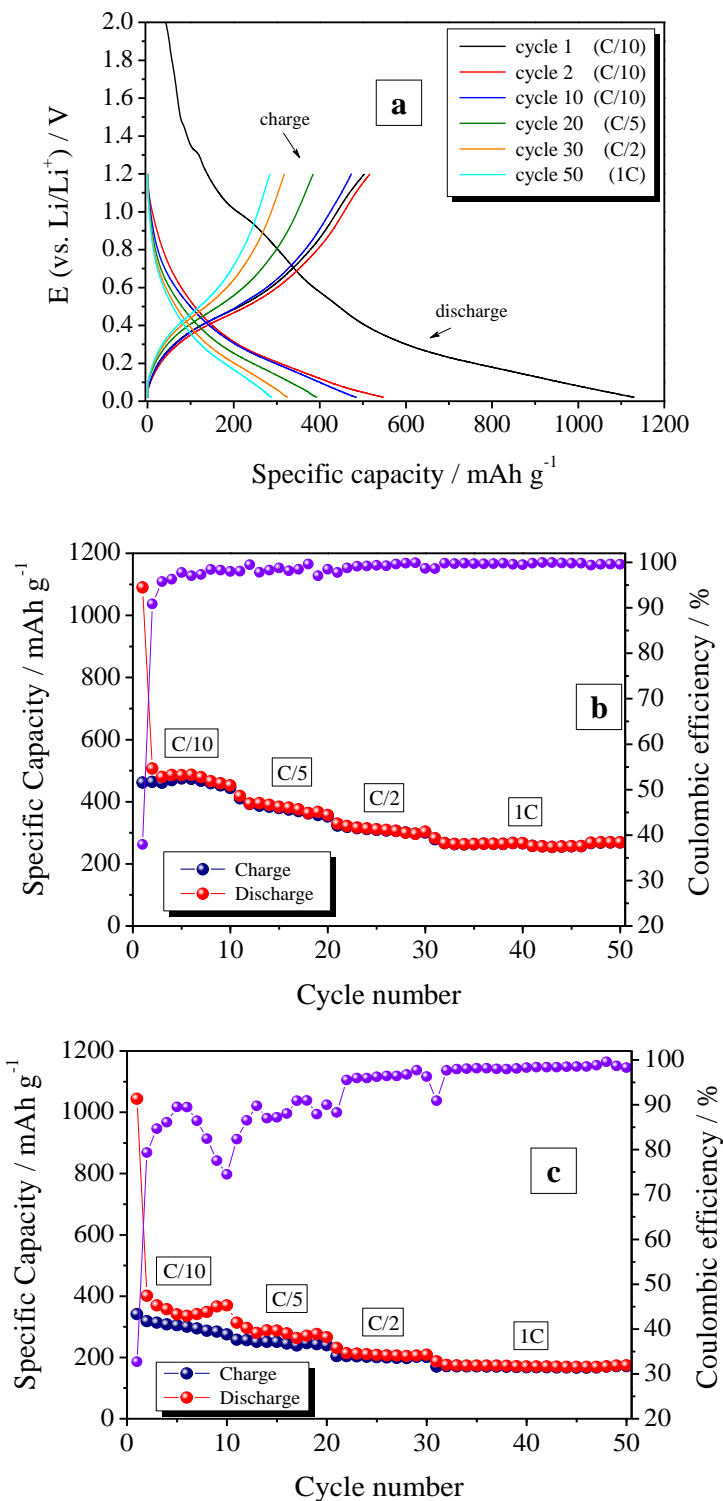


**Figure 5.** Constant current discharge/charge cycling test of the Li test cells at ambient temperature and at different current regimes: a) voltage profiles and b) specific discharge/charge capacities and coulombic efficiency with cycling of SnO<sub>2</sub>/MCS-P, c) specific discharge/charge capacities and coulombic efficiency of SnO<sub>2</sub>/MCS-S. The cycling tests consisted of a galvanostatic discharge/charge at C/10 rate (50 mA g<sup>-1</sup>) for the first 10 cycle, then at C/5 (100 mA g<sup>-1</sup>) for a period of 10 cycles, then at C/2 (250 mA g<sup>-1</sup>) for a period of 10 cycles, and, finally, at 1C (500 mA g<sup>-1</sup>) for a period of 20 cycles.

On measuring the charge/discharge capacity of the unsupported MCS-P (not shown here), we found out that it exhibits a reversible capacity of  $240 \text{ mAh g}^{-1}$  during the first cycle at C/10. Since the reversible specific capacity of the  $\text{SnO}_2/\text{MCS-P}$  electrode is  $462 \text{ mAh g}^{-1}$  during the first cycle, by subtracting the capacity of the mesoporous carbon component, the reversible specific capacity delivered by the  $\text{SnO}_2$  active particles (30.2 wt. %) has been estimated to be  $222 \text{ mAh g}^{-1}$ . Therefore, the specific capacity of  $\text{SnO}_2$  in the composite electrode has been calculated to be  $740 \text{ mAh g}^{-1}$ , corresponding to a very high 94.9 % of the theoretical value for  $\text{SnO}_2$ .

As already reported by Zhao et al. [24], such result demonstrates the beneficial effect of the mesoporous carbon support on the enhanced electrochemical performance of  $\text{SnO}_2$  electrodes. Indeed, the mesoporous structure of the carbon support can be very useful to limit the mobility and agglomeration of the Sn nanoparticles during cycling, as it buffers well against local volume changes in the Li-Sn alloying and de-alloying cycles. This is an excellent result as the main problem for tin-based alloys is the degradation of the electrode structure after prolonged cycling. Porosity and large surface area are favourable factors for the diffusion of lithium ions, providing more active sites. These result in significantly improved cyclability. Moreover, the mesoporous carbon matrix obtained by using phenanthrene as precursor should be also responsible for the improvement in the electronic conductivity of the composites.

In this respect, our experimental findings demonstrate that the kind of carbon precursor used exerts some influence. This has been verified by examining the cycling response of a similar  $\text{SnO}_2$  supported sample, in which the MCS support was prepared using sucrose instead of phenanthrene as carbon precursor. The electrochemical behaviour of this sample, namely  $\text{SnO}_2/\text{MCS-S}$ , is shown in Fig. 5c. By comparing Fig. 5b and 5c, it is clearly evident, especially at lower rates, the improvement in specific capacity, Coulombic efficiency and cyclability obtained in the case of  $\text{SnO}_2/\text{MCS-P}$ . Such behaviour suggests that the use phenanthrene improves the efficiency to cycling of the resulting anodic material, and can be ascribed both to changes in the mesoporous carbon structure or to an improvement of the carbon support electronic conductivity. "Ad hoc" tests will be carried out to put in evidence a possible relation between the kind of organic precursor used and the electronic conductivity of the resulting carbon support.

#### 4. CONCLUSIONS

In conclusion, we have demonstrated that  $\text{SnO}_2$  nanoparticles can be successfully supported into ordered mesoporous carbon spheres (MCS) leading to an interesting anode material for Li-ion cells. The wetness impregnation procedure used is very simple, with no critical parameters. The preliminary results obtained on the electrodes are very interesting from the scientific viewpoint because of the high utilization coefficient values. The important findings are that the dispersion into the pores of an open-structure mesoporous material enhances the electrochemical behaviour and, most probably, the use of phenanthrene as carbon precursor leads to a support with enhanced electronic conductivity. Moreover, the mesoporous structure of the carbon support can effectively buffer the volume changes during the Li-Sn alloying and de-alloying cycles. The as-prepared  $\text{SnO}_2/\text{MCS-P}$

nanocomposite electrode exhibited good cycling stability, with the specific capacity of SnO<sub>2</sub> in the composite electrode calculated to be 740 mAh g<sup>-1</sup>, corresponding to a very high 94.9 % of the theoretical value for SnO<sub>2</sub> (780 mAh g<sup>-1</sup>).

There are different ways of enhancing the electrochemical performances of the electrode to an application level, all of them actually followed by our research group. Major efforts are directed to increase the percentage of SnO<sub>2</sub> lodged onto the mesopores. In addition, one can choose an equally economical mesoporous material having pores on the three spatial directions. The extent of the initial irreversible capacity should be also maintained to the lowest possible level. Work is in progress in our laboratory to unravel the possible relation between the kind of organic precursor used and the electronic conductivity of the resulting carbon support.

#### ACKNOWLEDGEMENTS

The authors would like to thank Mr. Mauro Raimondo from Politecnico di Torino for the SEM-EDX analysis and Dr. M. Malandrino of the University of Turin for the ICP-AES analysis of the samples.

#### References

1. P.G. Bruce, B. Scrosati, and J.M. Tarason, *Angew. Chem. Int. Ed.*, 47 (2008) 2930
2. A.S. Aricò, P. Bruce, B. Scrosati, J.M. Tarascon, and W. van Schalkwijk, *Nat. Mater.*, 4 (2005) 366
3. D. Fauteux, and R. Koksang, *J. Appl. Electrochem.*, 23 (1993) 1
4. Y. Wang, F. Su, J.Y. Lee, and X.S. Zhao, *Chem. Mater.*, 18 (2006) 1347
5. J.M. Tarascon, and M. Armand, *Nature*, 414 (2001) 359
6. I.A. Courtney and J.R. Dahn, *J. Electrochem. Soc.*, 144 (1997) 2045
7. J. Hassoun, S. Panero, P. Reale and B. Scrosati, *Int. J. Electrochem. Sci.*, 1 (2006) 110
8. Y. Idota, Tadahiko Kubota, A. Matsufuji, Y. Maekawa, and T. Miyakasa, *Science*, 276 (1997) 1395
9. M. Winter, and J.O. Besenhard, *Electrochim. Acta*, 45 (1999) 31
10. M. Winter, J.O. Besenhard, M.E. Spahr, and P. Novak, *Adv. Mater.*, 10 (1998) 725
11. I. Grigoriants, L. Sominski, H. Li, I. Ifargan, D. Aurbach, and A. Gedanken, *Chem. Commun.*, (2005) 921
12. H.X. Zhang, C. Feng, Y.C. Zhai, K.L. Jiang, Q.Q. Li, and S.S. Fang, *Adv. Mater.*, 21 (2009) 2304
13. Z.H. Wen, Q. Wang, Q. Zhang, and J.H. Li, *Adv. Funct. Mater.*, 17 (2007) 2772
14. X.L. Ji, K.T. Lee, and L.F. Nazar, *Nature Mater.*, 8 (2009) 500
15. A. Katiyar, S. Yadav, P.G. Smirniotis, and N.G. Pinto, *J. Chromatogr. A*, 1122 (2006) 13
16. E.P. Ambrosio, C. Francia, C. Gerbaldi, N. Penazzi, P. Spinelli, M. Manzoli and G. Ghiotti, *J. Appl. Electrochem.*, 38 (2008) 1019
17. G.X. Wang, J. Yao, H.K. Liu, S.X. Dou, and J. Ahn, *Electrochim. Acta*, 50 (2004) 517
18. C. Gerbaldi, G. Meligrana, S. Bodoardo, A. Tuel, and N. Penazzi, *J. Power Sources*, 174 (2007) 501
19. K.S.W. Sing, D.H. Everett, R.H.W. Haul, L. Moscou, R.A. Pierotti, J. Rouquerol and T. Siemieniewska, *Pure Appl. Chem.*, 57 (1985) 603
20. D. Zhao, J. Feng, Q. Huo, N. Melosh, G.H. Fredrickson, B.F. Chmelka, and G.D. Stucky, *Science*, 279 (1998) 548
21. S.H. Joo, C. Pak, D.J. You, S.-A. Lee, H.I. Lee, J.M. Kim, H. Chang, and D. Seung, *Electrochim. Acta*, 52 (2006) 1618
22. S. Gómez, O. Giraldo, L.J. Garcés, J. Villegas, and S.L. Suib, *Chem. Mater.*, 16 (2004) 2411

23. H. Yang, G. Vovk, N. Coombs, I. Sokolov, and G.A. Ozin, *J. Mater. Chem.*, 8 (1998) 743
24. Z.W. Zhao, Z.P. Guo, P. Yao, and H.K. Liu, *J. Mater. Sci. Technol.*, 24 (2008) 657
25. H.P. Liu, D.H. Long, X.J. Liu, W.M. Qiao, L. Zhang, and L.C. Ling, *Electrochim. Acta*, 54 (2009) 5782
26. M. Mohamedi, S.-J. Lee, D. Takahashi, M. Nishizawa, T. Itoh, and I. Uchida, *Electrochim. Acta*, 46 (2001) 1161
27. D.-C. Rezan, Y.-S. Hu, M. Antonietti, J. Maier, and M.-M. Titirici, *Chem. Mater.*, 20 (2008) 1227
28. I. Sandu, T. Brousse, D.M. Schleich, and M. Danot, *J. Solid State Chem.*, 179 (2006) 476
29. J. O. Besenhard, M. Winter, J. Yang, and W. Biberacher, *J. Power Sources*, 54 (1995) 228